Journal of Materials Chemistry A

Accepted Manuscript

ROYAL SOCIETY OF CHEMISTRY

www.rsc.org/materialsA

Table of contents

Cambered nano-walls of SnO_2/rGO composites with controllable thickness were synthesized by using a recyclable melamine template.

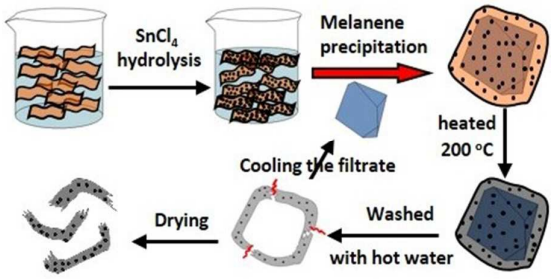

Journal Name

ARTICLE

Synthesis of Cambered Nano-walls of SnO_2/rGO Composites Using a Recyclable Melamine Template for Lithium-Ion Batteries

Received 00th January 20xx,
Accepted 00th January 20xx

DOI: 10.1039/x0xx00000x

www.rsc.org/

Rixing Shen[a], Yanzhong Hong[a], Joseph J. Stankovich[b], Zhiyong Wang[a], Sheng Dai[b] and Xianbo Jin[a*]

Graphene and graphene/metal oxide composite materials have attracted considerable interest for energy materials due to their excellent electrochemical performances. Here we propose using melamine as a template for the synthesis of cambered nano-walls of SnO_2/rGO materials. Melamine powder can effectively absorb SnO_2/GO from the solution to form a core-shell structure of melamine@SnO_2/GO. After thermal reduction of GO at 200 °C to form the melamine@SnO_2/rGO, melamine was dissolved in hot water at 80 °C, leaving behind the cambered SnO_2/rGO nano-walls. Melamine is recyclable since it precipitates when its solution cools to room temperature. The thickness of the SnO_2/rGO nano-walls can be easily controlled by adjusting the mass ratio of melamine to SnO_2/GO. When the mass ratio was set to ten, cambered walls of SnO_2/rGO with thickness of about 100-200 nm were achieved. The resulting SnO_2/rGO delivered an initial reversible capacity of at 998 mAh/g at a current density of 100 mA/g and a capacity of 855 mAh/g after 100 discharge-charge cycles in a potential range between 0.02 and 3.0 V vs. Li/Li^+. It also showed good rate performance with a reversible capacity of 460 mAh/g at 1A/g. These high capacities can be linked to the special cambered nano-walls which ensure fast solid diffusion in addition to providing an effective liquid-channel and buffer-volume in the electrode. The proposed synthesis method is easily scalable and should be applicable to many other graphene based energy materials.

1. Introduction

Li-ion batteries (LIBs) have attracted considerable attention for their high energy density and high average voltage. LIBs have a wide range of applications in electric/hybrid vehicles, portable electronic devices, and satellite equipments. [1-3] Great efforts have been made in exploring novel anode materials with superior cycling capacity and stability.[4-7] In recent years, nanocomposite materials composed of graphene and metal oxides, such as SnO_2, have become popular candidates of anode materials for LIBs.[8-10] Tin dioxide has high theoretical capacity (782mAh/g),[11,12] is low cost, and is nontoxic.[13,14] But pure SnO_2 is unsuitable for electrode applications since a volume change between Sn and $Li_{4.4}Sn$ during the lithiation/delithiation process can reach 359%. The volume changes often cause SnO_2 electrodes to crack and exhibit rapid capacity fading.[15,16] Graphene could be an ideal buffer material for SnO_2 in LIBs. It exhibits a number of intriguing properties including a perfect two-dimensional nanostructure, excellent electronic conductivity, high surface area (theoretical value 2600 m^2g^{-1}), and wide electrochemical window.[17-20] It was recently reported that SnO_2/graphene nanostructures may not only provide an effective volume buffer but also prevent the Sn nanoparticle from aggregation.[21-24]

However, the synthesis of high performance anode materials of nanostructured SnO_2/graphene remains challenging. The SnO_2/grapheme (often denoted as SnO_2/rGO in which the rGO represents graphene reduced from graphene oxide GO) has been typically derived from SnO_2/GO in an aqueous solution.[25-29] The drawbacks of this kind of synthesis include the use of expensive and hazardous reductants (such as hydrazine) and the aggregation of the nano-SnO_2/rGO.[30,31] Vacuum freeze drying and vacuum assisted thermal treatment are traditionally used to produce powders of SnO_2/rGO with an increased surface area and higher electroactivity, but these processes are time consuming and energy intensive.[32,33]

In this work, we demonstrate a simple method to prepare nano-walls of SnO_2/rGO composite with controllable thickness using melamine as a template. In this process, the dispersion of SnO_2/GO in aqueous solution is first precipitated by adsorbing onto the surface of the melamine powder to form a coating structure of melamine@SnO_2/GO. Next a thermal treatment of the melamine@SnO_2/GO is carried out at 200 °C for the reduction of GO to rGO. Finally, the melamine powder is dissolved by hot water, leaving behind the nano-walls of SnO_2/rGO as the product. Most of the melamine can be recovered by precipitation due to its lower solubility in water at room temperature. The initial reversible charge/discharge capacity of the resulting nano-walls of the SnO_2/rGO composite at a current density of 100 mAh/g can be as high as 995 mAh/g in the potential range between 0.02 and 3.00 V,

[a] College of Chemistry and Molecular Sciences, Hubei Key Laboratory ofElectrochemical Power Sources, Wuhan University, Wuhan, 430072, P.R. China.E-mail: xbjin@whu.edu.cn; Fax:+86-027-68756319; Tel:+86-027-68756319
[b] Oak Ridge National Laboratory, Oak Ridge, TN 37831, USA
† Electronic Supplementary Information (ESI) available.
SeeDOI: 10.1039/x0xx00000x

and approximately 850 mAh/g remained after 100 cycles, indicating high capacity and high cycling stability.

2. Experimental

2.1materials synthesis

Graphene oxide (GO) was synthesized from natural graphite powders via the Hummer's method.[34] After washing, centrifuging and drying, the GO was dispersed in deionized water under ultrasonication to form a GO solution with a concentration of 1mg/mL. Tin oxide (SnO_2) nanoparticles were obtained by hydrolysis of $SnCl_4$. For a typical synthesis of SnO_2/rGO nano-walls, 150mL GO solution (1mg/mL) was mixed with 50mL aqueous solution of $SnCl_4 \bullet 5H_2O$ (350mg) under stirring for 1.5 h to produce nanometer SnO_2/GO. Second, 1 to 5 g (corresponding to 3 to 17 in mass ratios of the melamine to SnO_2/GO) of melamine powder was added into the solution with stirring for another 1h at room temperature. After sedimentation and filtration, the brown precipitate of melamine@SnO_2/GO was collected and dried at 80 ^{o}C. Third, the melamine@SnO_2/GO was annealed at 200 ^{o}C for 2h to prepare the melamine@SnO_2/rGO. Finally, the melamine core was removed by rinsing three times with hot deionized water (80^{o}C and 100mL per rinse).The resulting SnO_2/GO nano-walls were collected and dried for further tests. The final product was notated as M(x)-SnO_2/rGO, where the M indicates the melamine template has been used during the material synthesis, and the x changes from 1 to 5 corresponding to the mass of melamine added. As a reference, x = 3 means the mass ratio of the melamine to SnO_2/GO is 10. For comparison, a SnO_2/rGO sample was synthesized in the same way without the addition of melamine. The nanometer SnO_2 was synthesized by hydrolysis of $SnCl_4$.

2.2 Characterization

The powder X-ray diffraction (XRD, Shimadzu XRD-6000 Cu Kα radiation) was used for the structural characterization. The data were collected between scattering angles (2θ) of 10-80°at a scanning rate of 4°/min. The scanning electron microscopy (SEM, Quanta 200, FEI) and transmission electron microscopy (TEM, JEOL JEM-2010FEF) were conducted for the morphology observation. X-ray photoelectron spectroscopy (XPS) analysis was carried out with a Thermo Fisher ESCALAB 250xi Ultra spectrometer with an Al Kα excitation source. The weight percentage of SnO_2 in nanocomposite was determined by thermogravimetric analysis (TGA Q500, TA Instrument) scanning from 100 to 800 ^{o}C at an average rate of 10 ^{o}C/min in air. Fourier-transform IR (FTIR) spectra of the samples were recorded using a Nicolet-MEXUS 670 Spectrophotometer. Raman analysis was performed with a Jobin Yvon HR800 Raman spectrometer. The Brunauer, Emmett and Teller (BET) surface area was analyzed by Micromeritics ASAP 2020 Analyzer (Norcross, GA) with nitrogen adsorption.

2.3 Electrochemical tests

The electrochemical properties of the active materials (the M(x)-SnO_2/rGO) and the reference material were studied in 2016-type coin cells with lithium metal foil as a counter electrode. The electrolyte is 1M $LiPF_6$/EC+DMC+DEC (v/v/v, 1:1:1). The separator of cell was Celguard 2400. The test electrodes were nickel foam supported rolled membranes (0.1 mm thick and *ca.* 3 mg/cm^2) comprising 70 wt% active material and 20 wt% acetylene black plus 10 wt% polytetrafluoro-ethylene (PTFE), which have a diameter of 10 mm. The cells were assembled in a glove box filled with argon gas (VAC OMNI-lab). Charge–discharge cycling of the coin cell was galvanostatically performed at room temperature with cut-off voltages of 0.02 V and 3.00 V, controlled by the BTS-55 Neware Battery Testing System (Shenzhen, China). In this study, the charging and discharging processes represent Li-dealloying and Li-alloying processes, respectively. The cyclic voltammograms (CVs) were carried out using a CHI660a potentiostat. The electrochemical impedance spectra was recorded at 2.0 V by applying an AC signal of 10 mV in the frequency range from 100 kHz to 0.01 Hz.

3. Results and discussion

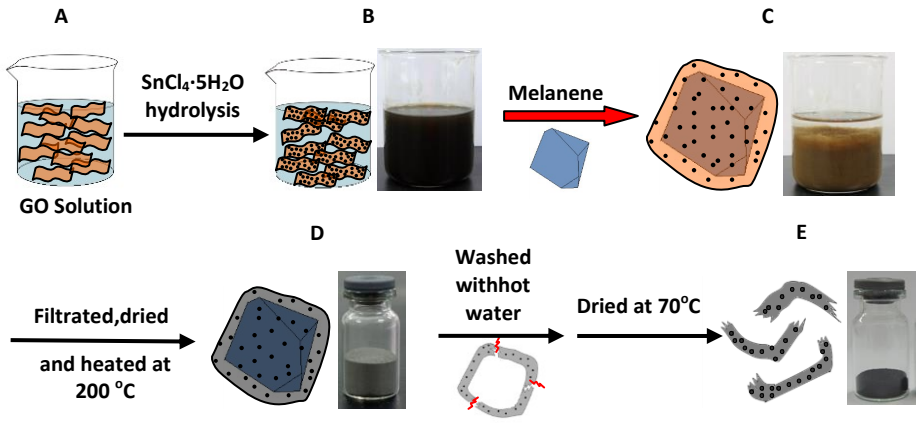

Fig. 1 Schematic illustration of the synthesis of nano-walls of nano-SnO_2/rGO.

The process of synthesizing nano-walls of nano-SnO_2/rGO is illustrated in Fig. 1. Graphene oxide has plenty of epoxy, hydroxyl and carboxylic acid groups, and it can be well dispersed in water (Fig. 1A). [35-37] It was previously reported that the hydrolysis of Sn^{4+} ions in the presence of GO yields a uniform coating of nano-SnO_2 particles on the graphene oxide layers.The Sn^{4+} ions can be attracted and anchored by the oxygenic groups of GO and the generated SnO_2 nanoparticles can bond with the oxygenic groups through hydrogen bonding interaction.[38] Here, a well dispersed suspension solution of SnO_2/GO (Fig. 1B) was generated. The addition of melamine powders into the suspension solution resulted in a pale brown precipitate which could be easily collected through filtration. The upper layer solution became clear (Fig. 1C), indicating all the SnO_2/GO particles might have been absorbed by the melamine powders, probably though the hydrogen bonding between the $-NH_2$ groups of melamine and the oxygenic groups of GO and forming a coating structure of melamine@SnO_2/GO. To confirm this, the SEM images of the melamine powder before and after the codeposition were observed. The original melamine consisted of particles with smooth surfaces and diameters between 10-50 μm (Fig. 2a). The morphology of the melamine powders was almost unchanged after soaking in pure water at room temperature (Fig. S1). However the surfaces of the melamine@SnO_2/GO particles were rough, suggesting the coating of SnO_2/GO on the melamine particles. Additionally, the average particle size of the melamine@SnO_2/GO was also larger than that of the melamine particles. Some of the melamine@SnO_2/GO particles were much larger, likely due to aggregation after the coating of SnO_2/GO on the melamine particles.

Since GO could be reduced to rGO by decomposition at temperatures higher than 180 °C, [39,40] the melamine@nano-SnO_2/GO powder was heated at 200 °C for 2h. After thermal treatment, the brown color of the melamine @nano-SnO_2/GO changed to a grey black (Fig. 1D), suggesting the reduction of GO to rGO. The melamine in the materials was then removed by washing with hot water (~80 °C), leaving behind the black fluffy powder of nano-walls of nano-SnO_2/GO (Fig. 1E). It was found that melamine precipitated from the solution after the filtrate cooled in air, obviously due to the much lower solubility of the melamine in cold water. After filtration, about 67% of melamine was recovered for the synthesis of the M(3)-SnO_2/rGO. Considering the solubility of melamine in water at ambient temperature (~ 15°C) is about 0.25 wt%, [41] it is believed the other 33% of melamine (about 1g) remained in the total 500 ml filtrate and was the result of the synthesis and washing. However, the filtrate could be used for the next synthesis of M(x)-SnO_2/rGO.

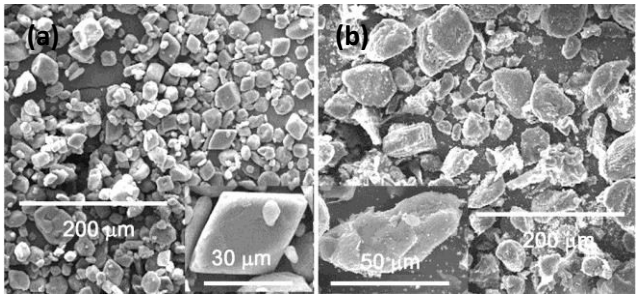

Fig. 2 SEM images of the melamine powders before (a) and after (b) soaking in the SnO_2/GO suspension solution.

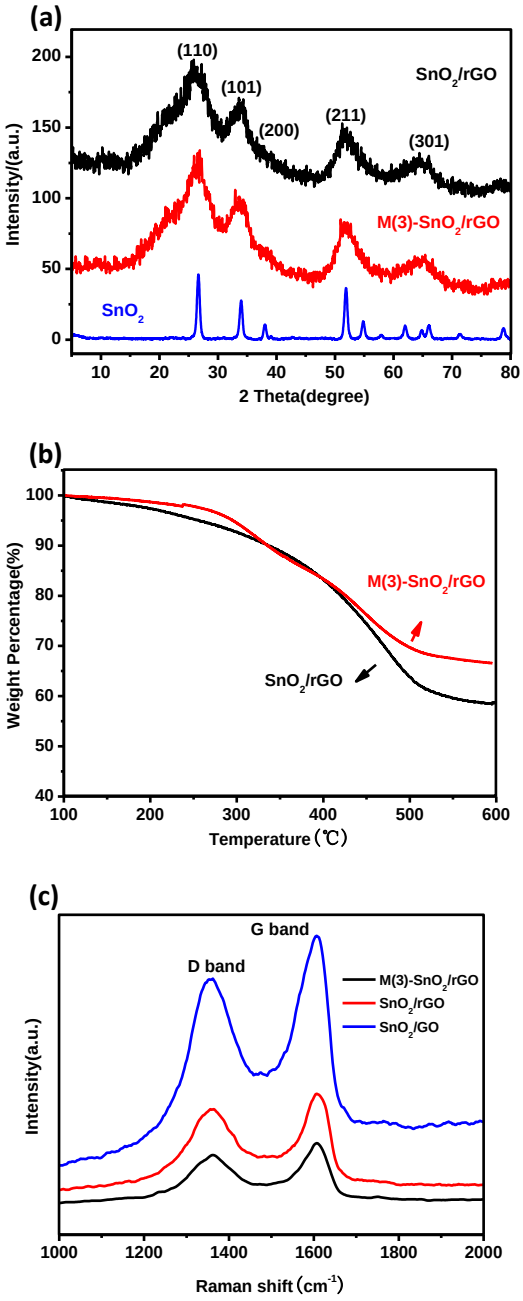

Fig. 3 (a) X-ray diffraction (XRD) patterns of M(3)-SnO_2/rGO, SnO_2/rGO and pure nanometer SnO_2. (b) Thermogravimetric Analysis (TGA) of M(3)-SnO_2/rGO and SnO_2/rGO. (c) Raman spectra of the M(3)-SnO_2/rGO, SnO_2/rGO and SnO_2/GO composites.

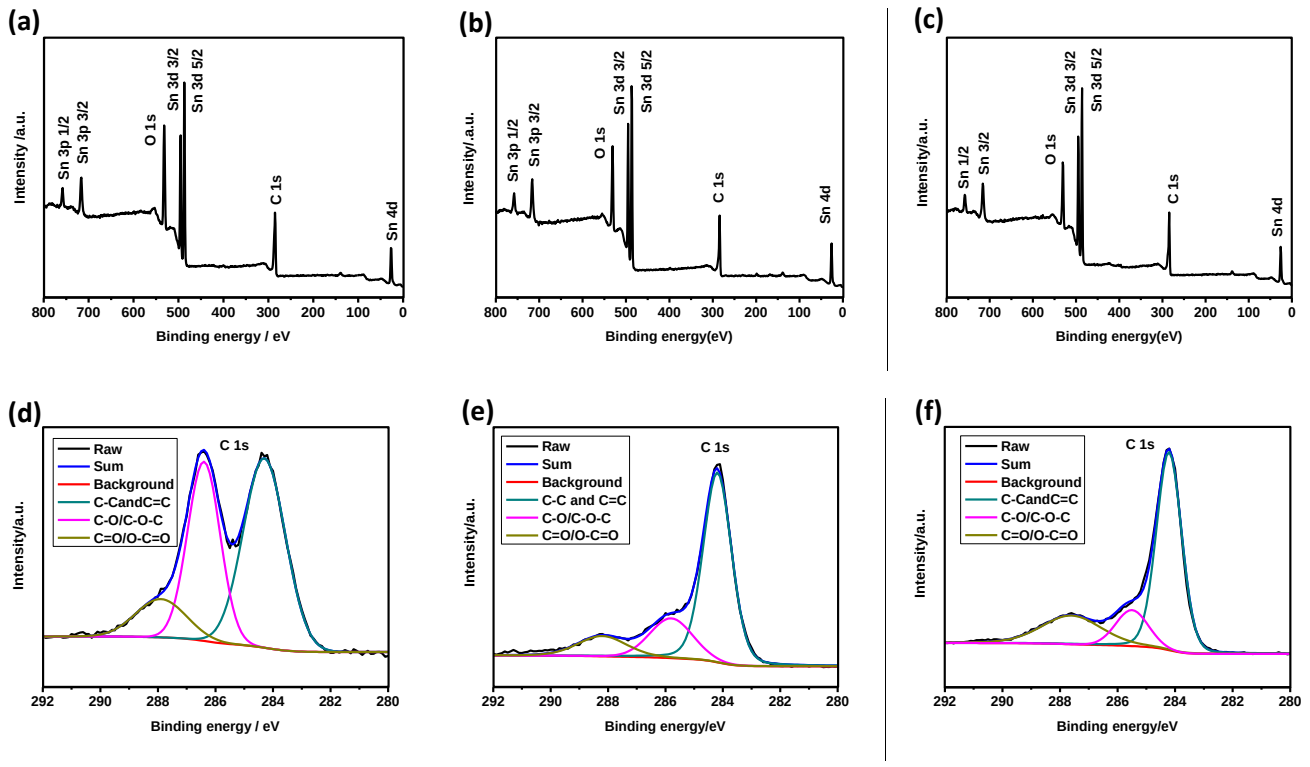

Fig.4 Wide XPS spectra of (a) SnO_2/GO, (b) SnO_2/rGO and (c) M(3)-SnO_2/rGO and the respective high resolution C1s spectra of (d) SnO_2/GO, (e) SnO_2/rGO and (f) M(3)-SnO_2/rGO.

The XRD patterns of M(3)-SnO_2/rGO, SnO_2/rGO and bare SnO_2 are compared in Fig. 3a. The XRD pattern of pure SnO_2 showed a tetragonal phase (JCPDS card no. 41-1445), in which, the 110, 101, and 211 peaks were distinct and sharp. However, the XRD patterns of M(3)-SnO_2/rGO and SnO_2/rGO were similar, and their diffraction peaks were broad and weak, indicating the small particle size of the SnO_2 in the composite materials.[22] The Scherrer formula was used to calculate the particle size of SnO_2; from the 211 and 301 peaks it was determined the particle size of SnO_2 was 2.4 nm. The broad peak at 24° corresponds to the amorphous structure of graphene. The weight percentage of SnO_2 in M(3)-SnO_2/rGO and SnO_2/rGO were about 66 wt.% and 59 wt.% respectively according to the thermo-gravimetric analysis (TGA, Fig. 3b), noting that the final mass after calcination of these composite materials in air would be pure SnO_2.

The thermal reduction of GO to rGO during the treatment at 200 °C was initially confirmed by Raman analysis (Fig. S2a). Fig. 3c shows the Raman spectra of carbon in different composites, including a G peak at about 1610 cm^{-1} due to the bond stretching of sp^2 atoms and a D peak at about 1360 cm^{-1} as an indication of defects on the graphitic plane. The intensity ratio of the D to G peak (I_D/I_G) of the SnO_2/GO sample was about 0.80, which increased to 0.86 of M(3)-SnO_2/rGO and 0.85 of SnO_2/rGO, revealing increased defects in the carbon structure after the heat treatment, in agreement with the fact that a heat de-composition of GO would increase vacancies within the graphene plane and defects at the boundaries.[42]

The thermal reduction of GO was also manifested by XPS analysis. Fig.4a, b and c show wide XPS survey spectra of SnO_2/GO, SnO_2/rGO and M(3)-SnO_2/rGO respectively. As expected, the peaks of C(1s), O(1s) and Sn(3p, 3d, 4d) emerged. The corresponding high resolution C1s peaks are shown in Figure 4d, e and f respectively, which were deconvoluted to three peaks at 284.2, 285.5 and 287.6 eV. These peaks are usually assigned to the unoxidized graphite carbon skeleton (C-C, C=C), hydroxyl or epoxide group (C-OH, C-O-C), and carboxyl group(C=O), respectively.[36,43,44] It can be seen that after the thermal treatment at 200 °C for 2 h, the oxygenic groups in the GO decreased significantly. The carbon to oxygen atomic ratio $R_{C/O}$ in the graphitic walls of SnO_2/GO was calculated to be about 2.3:1, which increased to about 7.4:1 in M(3)-SnO_2/rGO and 6.0:1 in the SnO_2/rGO. The XPS results also suggested that the reduction of GO in these materials was mainly caused by the heat. It is likely that the melamine has only taken a small part, if any, in the reduction of GO. There are other indications that melamine is inert. For example, the thermal treatments led to a similar degree of reduction to both melamine@SnO_2/GO and SnO_2/GO; there is almost no signal of N in the XPS spectrum of M(3)-SnO_2/rGO (Fig. 4c). In addition, the FTIR spectra of the original melamine and the recovered melamine from melamine@SnO_2/rGO were almost identical (Fig. S2b), indicating the oxidation to the

$-NH_2$ was negligible. The M(3)-SnO_2/rGO had a relatively lower oxygen content, probably because the thinner thickness of the SnO_2/GO layer on melamine should be beneficial for reduction during the heat treatment.

To investigate the influence of melamine on the morphology of the products, scanning electron microscopic (SEM) observations were carried out. As can be seen from Fig. 5a, without adding melamine, the SnO_2/rGO had a high degree of aggregation. The M(x)-SnO_2/rGO samples with x between 2 and 5 all consisted of cambered walls. This kind of shape corresponds to the occurrence of a rupture of the coating layer during removal of the melamine core from the melamine@SnO_2/GO, as illustrated in Fig. 1. Fig. 5 also indicates that the wall thickness of the M(x)-SnO_2/rGO was controlled by the usage amount of melamine. The M(2)-SnO_2/rGO exhibited a thickness of about 1 μm (Fig. 5b).The thickness of the M(3)-SnO_2/rGO decreased significantly to about 100~200 nm (Fig. 5c). Since the usage of melamine in M(3)-SnO_2/rGO was only 1.5 times of that in M(2)-SnO_2/rGO, the great difference in wall thicknesses between the two samples can be attributed to the slight dissolution of melamine as aforementioned. It can be seen that the wall thickness of the M(5)-SnO_2/rGO decreased further (Fig. 5d). When more melamine particles were added the coating layer of the SnO_2/rGO on the particle surface should be thinner. The morphology difference between SnO_2/rGO and M(x)-SnO_2/rGO were in line with the results of the Brunauer–Emmett–Teller (BET) analysis. For example, the BET surface area of SnO_2/rGO and M(x)-SnO_2/rGO were found to be about 40 and 146 m^2/g respectively (Fig. S3), indicating that the melamine template method was an effective way to achieve a high surface area for hybrid materials.

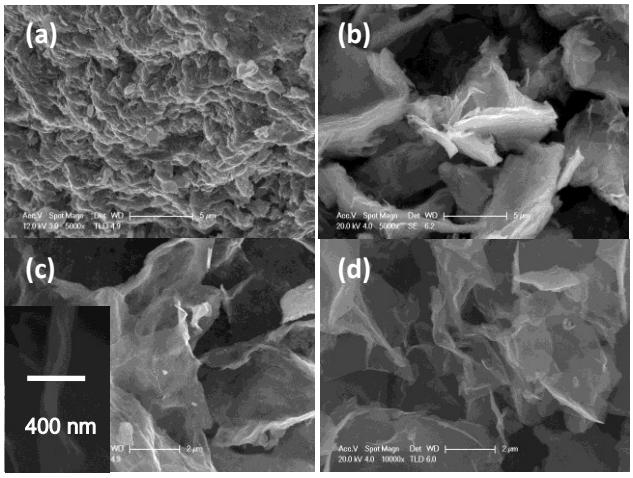

Fig. 5 SEM images of (a)SnO_2/rGO, (b) M(2)-SnO_2/rGO, (c) M(3)-SnO_2/rGO (the inset shows a perpendicular wall) and (d) M(5)-SnO_2/rGO.

The aggregation of SnO_2/rGO and cambered thin sheets of M(x)-SnO_2/rGO have also been observed under transmission electron microscope (TEM) (Fig. S4). The high resolution TEM (HRTEM) images of SnO_2/rGO and M(3)-SnO_2/rGO are shown in Fig. 6, indicating that uniform nanocrystals of SnO_2 were distributed homogeneously in both samples. The particle sizes of SnO_2 in SnO_2/rGO (Fig. 6a) and M(3)-SnO_2/rGO (Fig. 6b) were also similar. However, Fig. 6a shows many overlapping SnO_2 particles, most likely due to the high degree of aggregation of SnO_2/GO particles during the drying and thermal reduction processes. Conversely, individual SnO_2 particles in the nano-walls of M(3)-SnO_2/rGO can be easily identified according to the clearer lattice fringes displayed in Fig. 6b. It can be determined that the SnO_2 particles in M(3)-SnO_2/rGO were about 2.5~4 nm. The small particle sizes were in agreement with the XRD and the selected area diffraction (SAED) patterns both showing weak diffraction intensity of SnO_2.

Fig.7a compares the charge capacities of M(x)-SnO_2/rGO (x=1, 2, 3, 5), SnO_2/rGO and bare SnO_2 during cycling in a voltage range of 0.02-3 V (vs Li/Li^+) at a current density of 100 mA/g over 100 cycles at room temperature. The capacities of all materials fade faster in first five cycles

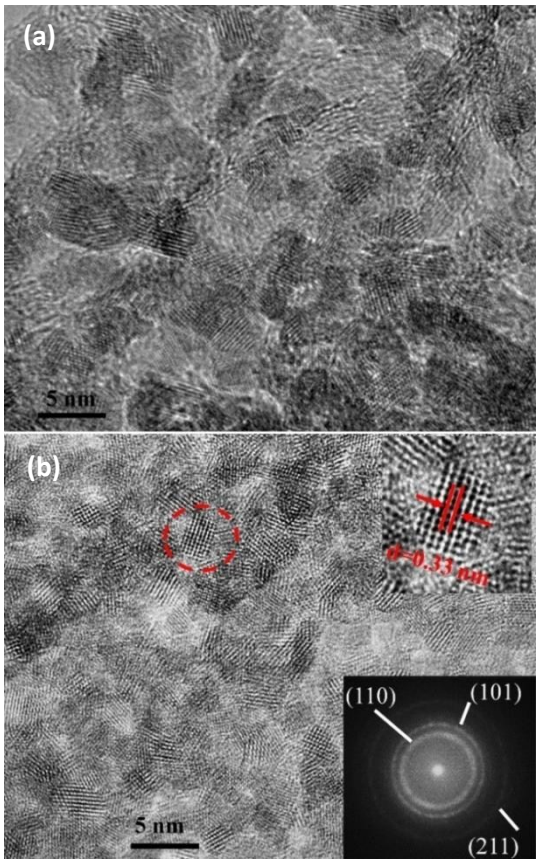

Fig. 6 HRTEM images of (a)SnO_2/rGO and (b)M(3)-SnO_2/rGO. The insets in (b) show the corresponding SAED pattern of (b) and the enlarged HRTEM image of the circled particle respectively.

due to the formation of SEI layer and the partially reversibility reduction of SnO_2 to Sn + Li_2O. The bare SnO_2 consisted of nanoparticles with an average size of about 10 nm, and displayed an aggregate morphology under SEM and TEM observations (Fig. S5).[31] Although the bare SnO_2 delivered an initial charge capacity of 885 mAh/g, it showed a poorest cycling stability and a lowest charge capacity (~30 mAh/g) at the 100th cycle. This is expectable for it is well-known that anode of pure SnO_2 suffers from huge volume changes during cycling leading to the pulverization of the electrode.

Compared with bare SnO_2, the SnO_2/rGO composite had much better performance, due to the good dispersion of SnO_2 nanoparticles among the rGO, which provided a buffer to the volume expansion and the good electrical conductivity.[22] However the SnO_2/rGO may suffer from aggregation as observed under SEM (Fig. 5). The addition of the melamine template to synthesize cambered walls of M(x)-SnO_2/rGO showed a positive effect to the performance, and the more the melamine added, the better the performance of the resulting material (Table S1). Undeniably the M(3)-SnO_2/rGO and M(5)-SnO_2/rGO composite showed the best cycling stability and the highest discharge capacity among the six samples. The charge capacity of SnO_2/rGO at the 100th cycle was about 536 mAh/g, a value similar to that reported for directly dried SnO_2/rGO after filtration from solution.[45] In comparison, the M(3)-SnO_2/rGO delivered a capacity of 855 mAh/g at the 100th cycle, which was as high as 810 mAh/g even at the 150th cycle, much greater than that of SnO_2/rGO.

The corresponding coulombic efficiency of M(3)-SnO_2/rGO, SnO_2/rGO, and SnO_2 are displayed in Fig. 7b. The coulombic efficiency of the M(3)-SnO_2/rGO increased from the initial 64% to about 94% in the second cycle, and later increases to about 100% after about 10 cycles. The M(3)-SnO_2/rGO showed a much higher initial coulombic efficiency than those of SnO_2/rGO (44.2%) and SnO_2 (47.9%).

The M(3)-SnO_2/rGO also showed a good cycling performance at a higher charge/discharge current of 0.5 A/g (Fig. S6). It delivered reversible capacities of about 900 and 670 mAh/g at initial and at the 150th cycle respectively. In comparison, the capacity of SnO_2/rGO decayed from 530 mAh/g at initial to about 250 mAh/g at the 150th cycle, indicating much poorer capacity and cycling stability.

The excellent cyclic ability should be ascribed to that in the nanostructure of M(3)-SnO_2/rGO, rGO should work as a good barrier to prevent the Sn nanoparticles from aggregation. Indeed, the TEM image (Fig. S7) did show that the particle size of Sn or SnO_2 in the M(3)-SnO_2/rGO sample remained less than 5 nm after 100 charge/discharge cycles. The EDX elemental mappings as shown in Fig. 8 also confirmed that the Sn and O elements were distributed uniformly in the graphene matrix, indicating no obvious aggregation occurred during the cycling.

The M(3)-SnO_2/rGO was further investigated by CVs. Fig. 9a displays the recorded CV curves of M(3)-SnO_2/rGO over a voltage range of 0.01-3.00V versus Li/Li^+. Oxidation and

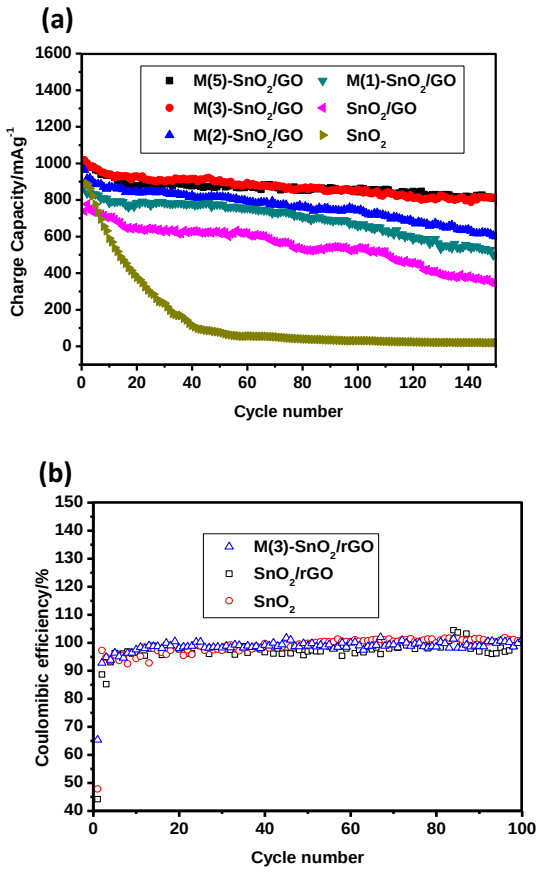

Fig. 7 (a) Plots of charge capacities of M(x)-SnO_2/rGO (x=1, 2, 3, 5), SnO_2/rGO composite and bare SnO_2 during cycling at a current density of 100 mA/g between 0.02-3.00V.(b) The corresponding coulombic efficiencies of charge and discharge of several samples in (a).

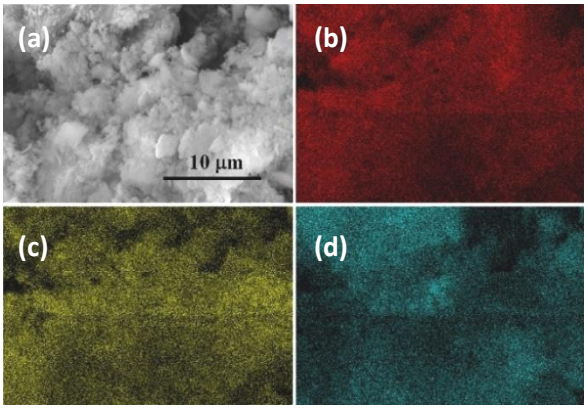

Fig. 8 (a) SEM image of M(3)-SnO_2/rGO sample torn off from the electrode and EDX elemental mapping spectra of C (b), O (c) and Sn (d) after 100 charge/discharge cycles at 100 mA/g.

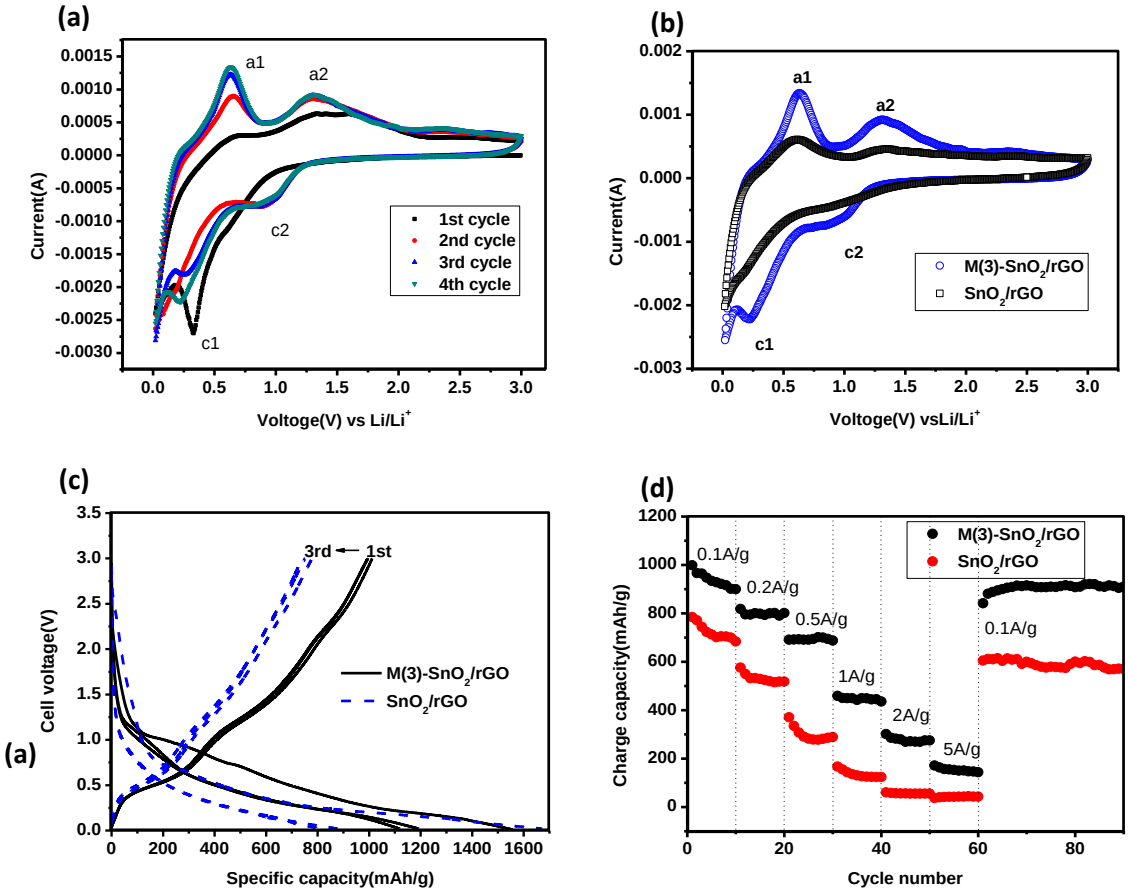

Fig. 9 (a) Cycle Voltammograms (CVs) of M(3)-SnO_2/rGO at a scan rate of 0.1mV/s and (b) compares the 4th cycle CVs of M(3)-SnO_2/rGO and SnO_2/rGO at a scan rate of 0.1mV/s. (c) the recorded 1st to 3rd charge and discharge curves of M(3)-SnO_2/rGO and SnO_2/rGO at current density of 100 mA/g between 0.02-3.00V. (d) Rate performances of M(3)-SnO_2/rGO and SnO_2/rGO composites.

reduction currents in first and second cycles of scanning were relatively small probably due to the electrode not being saturated with the electrolyte. The CVs became almost producible from the third cycle. The highly reversible redox peaks c1 at 0.23 V and a1 at 0.63 V can be attributed to Li-alloying and Li-dealloying respectively, which contributed to most of the capacity of a SnO_2 based electrode traditionally.[36,46] The cathodic peak at a potential about 0.93 V (c2) was usually attributed to the formation of the SEI layer, as well as the reduction of the SnO_2 to Sn and Li_2O (SnO_2+ $4Li^+$+4e=$2Li_2O$ + Sn).[47,48] This reduction reaction was as partially reversible.[16,47] In our case, the corresponding anodic peak a2 at 1.31 V with a tail leveled off until about 2.2 V suggesting a slow reverse reaction of c2.[36,46] However, the a2 is still remarkable, suggesting good reversibility of the c2/a2 couple of the M(3)-SnO_2/rGO material.

However, there were many differences in CVs between M(3)-SnO_2/rGO and SnO_2/rGO, which suggested the advantages of the M(3)-SnO_2/rGO (Fig. 9b). First, both the redox peaks of c1/a1 and c2/a2 couples of the M(3)-SnO_2/rGO were well shaped compared to those of SnO_2/rGO. Second, the c1/a1 and c2/a2 currents of M(3)-SnO_2/rGO peaked at 0.23 V/0.63 V and 0.93 V/1.31 V respectively, while those of SnO_2/rGO peaked at 0.18 V/0.62 V and 0.85V/1.33V respectively. These suggest both c1/a1 and c2/a2 couples of M(3)-SnO_2/rGO were more reversible than those of SnO_2/rGO. Particularly, The potential difference between a2 and c2 (0. 38 V) of M(3)-SnO_2/rGO was much smaller than that (0.48 V) of SnO_2/rGO, indicating the cambered nano-wall structure can help to increase the reversibility of the conversion reaction between SnO_2 and Sn+Li_2O, resulting in the much greater cycling capacity than that of SnO_2/rGO.

The enhanced reversibility of the conversion reaction could be the reason for the higher capacity of M(3)-SnO_2/rGO than that of both rGO and traditional SnO_2. The experimental cycling capacity of rGO was reported to be 300~500 mAh/g.[36] When taking only the Li-alloying of Sn into account, the theoretical reversible capacity of SnO_2 is 782 mAh/g. Consequently, considering the 66% weight percentage of SnO_2 in M(3)-SnO_2/rGO and assuming a capacity of 400 mAh/g of rGO, the capacity of M(3)-SnO_2/rGO could be estimated to be about 650 mAh/g. However, this capacity could reach at 1120 mAh/g if both the conversion reaction between SnO_2 and Sn+Li_2O and the

Li-alloying reaction of Sn in M(3)-SnO_2/rGO could be fully reversible (in such case, the theoretical capacity of SnO_2 alone becomes to be 1494 mAh/g). As shown in Fig. 7a, M(3)-SnO_2/rGO delivered a capacity 1000 mAh/g at initial and 855 mAh/g at the 100th cycle, which lay between 650 and 1120 mAh/g, suggesting that a significant part of the capacity arising from the conversion reaction should be reversible. This may be true according to the CVs in Fig 9a, showing distinct c2/a2 redox peaks of the conversion reaction with considerable peak areas compared to that of the alloying reaction (c1/a1).

The galvanostatic discharge-charge curves of M(3)-SnO_2/rGO and SnO_2/rGO were compared in Fig. 9c. The potential plateau about 0.75V (vs.Li/Li^+) in the first cathodic process of M(3)-SnO_2/rGO should corresponds to mainly the irreversible reduction of SnO_2 to Sn + Li_2O, together with the formation of SEI membranes.[47,48] From the second cycle, in line with the CVs in Fig. 9a, the cathodic branch shows two main stages, which centered at 0.9 V and 0.25 V respectively. The first stage may correspond to the reduction of SnO_2, and the second one may include mainly Li-alloying reactions of both SnO_2 and graphene.[36] The anodic branches show two corresponding charging plateaus, at about 1.4 V and 0.5 V respectively. In comparison, the SnO_2/rGO showed no or less charging and discharging plateau at potentials above 0.7 V, suggesting the con-version reaction between SnO_2 and Sn + Li_2O had insignificant contribution to the cycling capacity of SnO_2/rGO. In addition, the SnO_2/rGO showed higher charging potential but lower discharging potential compared to those of M(3)-SnO_2/rGO, indicating greater polarizations in the SnO_2/rGO electrode.

In order to investigate the potential application for high power lithium-ion batteries, the rate performances of M(3)-SnO_2/rGO and SnO_2/rGO were tested at current densities ranging from 100 to 5000 mA/g (Fig.8d). The M(3)-SnO_2/rGO displayed an excellent rate capability. It delivered charging capacities of about 900, 800, 700, 460, 270, and 150 mAh/g at 100, 200, 500, 1000, 2000, and 5000 mA/g, respectively. When the current was set back to 100 mA/g, a capacity of 900 mAh/g could be restored and kept stable in the subsequent cycles. This rate capability was much better than that of SnO_2/rGO which delivered charge capacities of about 530, 290, 130, 55, and 40 mAh/g at 200, 500, 1000, 2000 and 5000 mA/g respectively.

AC impedance analysis was also carried out to understand the benefits of the M(3)-SnO_2/rGO composite over SnO_2/rGO. The AC impedance spectra in Fig. S8 were obtainedunder similar conditions, indicating that the charge transfer resistance (7 Ω) of the M(3)-SnO_2/rGO electrode was much smaller than the 18 Ω of the SnO_2/rGO electrodes, likely due to that the former had a larger electrolyte/active material contact area. The solid diffusion coefficient of Li^+ ions in the M(3)-SnO_2/rGO electrode can be derived from the Warburg impedances in the low frequency range, which was calculated to be 2.0×10^{-9} cm^2s^{-1}, much greater than that ($0.8 \times 10^{-9}cm^2s^{-1}$) in the SnO_2/rGO electrode. The excellent performances of M(3)-SnO_2/rGO can then be attributed to its two structure advantages: (1) the thin walls of SnO_2/rGO would be preferable for the solid ion diffusion during lithiation/delithiation processes, and (2) their cambered structure may prevent the walls from a close packing, hence provide many liquid ionic channels, large electro-chemical surface area and effective buffer volume.[49,50] These structure advantages have led to performances of the composites comparable to the best of the SnO_2/rGO reported in most recent literatures.[25,43,51-57] It is hopeful to further improve the performance by combining the cambered Nano-walls structure with other chemical modifications, such as nitrogen doping of SnO_2/rGO composites.[21, 58-60]

4. Conclusion

We demonstrated using melamine as a recyclable template for the synthesis of cambered nano-walls of SnO_2/rGO composites (M(x)-SnO_2/rGO). The synthesis route included four steps: preparation of SnO_2/GO solution by hydrolysis of $SnCl_4$ in GO solution; adsorption of the SnO_2/GO on the surface of melamine to form a core-shell structure of melamine@SnO_2/GO; thermal reduction of GO at 200 ^oC to form the melamine@SnO_2/rGO; finally removal of the melamine core by dissolving in hot water at about 80^oC with SnO_2/rGO coating layer cracking to cambered walls. It was found that the melamine is a good adsorbent for M(x)-SnO_2/rGO. Melamine dissolves in hot water and precipitates when the solution cools; this makes it a perfect recyclable template. The wall thickness of the M(x)-SnO_2/rGO can be easily controlled by adjusting the amount of melamine powder added into the SnO_2/GO solution, and cambered walls of SnO_2/rGO with thickness down to under 100 nm have been achieved. TEM observation indicated that SnO_2 nanoparticles with sizes of about 2.5-4 nm uniformly dispersed among the nano-wall matrix of rGO were achieved. When used for lithium ion batteries, the M(x)-SnO_2/rGO with wall thickness of about 100-200 nm performed much better than the SnO_2/rGO prepared using the similar method without the melamine template. The enhanced performances were thought to arise from the special cambered nano-wall structure of the materials that allows fast solid diffusion and easy liquid mass transfer, and provides an effective volume buffer. The proposed synthesis method is simple in operation, environmentally friendly, inexpensive, and energy saving. It is easily scalable. The presented strategy should be applicable to the fabrication of cambered nano-walls of many other graphene based energy materials.

Acknowledgements

This work is supported by NSFCs (21173161), the MOE Program (NCET-11-0397), the Fundamental Research Funds for the Central Universities of Wuhan University.

Notes and references

1 M. Armand and J. M. Tarascon, *Nature*, 2008, **451**, 652-657.
2 M. Liang and L. Zhi, *Journal of Materials Chemistry*, 2009, **19**, 5871.
3 S. M. Paek, E. Yoo and I. Honma, *Nano Letters*, 2009, **9**, 72-75.
4 J. Luo, X. Xia, Y. Luo, C. Guan, J. Liu, X. Qi, C. F. Ng, T. Yu, H. Zhang and H. J. Fan, *Advanced Energy Materials*, 2013, **3**, 737-743.
5 D. Liu, B. B. Garcia, Q. Zhang, Q. Guo, Y. Zhang, S. Sepehri and G. Cao, *Advanced Functional Materials*, 2009, **19**, 1015-1023.
6 Y. Chen, B. H. Song, R. M. Chen, L. Lu and J. M. Xue, *Journal Of Materials Chemistry A*, 2014, **2**, 5688-5695.
7 Y. Liu, D. Liu, Q. Zhang, D. Yu, J. Liu and G. Cao, *Electrochimica Acta*, 2011, **56**, 2559-2565.
8 C. N. Rao, A. K. Sood, K. S. Subrahmanyam and A. Govindaraj, *Angewandte Chemie*, 2009, **48**, 7752-7777.
9 Z. Wang, D. Luan, F. Y. Boey and X. W. Lou, *Journal of the American Chemical Society*, 2011, **133**, 4738-4741.
10 J. S. Chen, L. A. Archer and X. Wen Lou, *Journal of Materials Chemistry*, 2011, **21**, 9912.
11 Z. Chen, M. Zhou, Y. Cao, X. Ai, H. Yang and J. Liu, *Advanced Energy Materials*, 2012, **2**, 95-102.
12 X. W. Lou, C. M. Li and L. A. Archer, *Advanced Materials*, 2009, **21**, 2536-2539.
13 X. W. Lou, D. Deng, J. Y. Lee and L. A. Archer, *Chemistry Of Materials*, 2008, **20**, 6562-6566.
14 Y. Idota, T. Kubota, A. Matsufuji, Y. Maekawa and T. Miyasaka, *Science*, 1997, **276**, 1395-1397.
15 P. Meduri, C. Pendyala, V. Kumar, G. U. Sumanasekera and M. K. Sunkara, *Nano Letters*, 2009, **9**, 612-616.
16 J. S. Chen and X. W. Lou, *Small*, 2013, **9**, 1877-1893.
17 G. Hong, Q.-H. Wu, J. Ren, C. Wang, W. Zhang and S.-T. Lee, *Nano Today*, 2013, **8**, 388-402.
18 C. Wang, Y. Li, Y. S. Chui, Q. H. Wu, X. Chen and W. Zhang, *Nanoscale*, 2013, **5**, 10599-10604.
19 B. Lu, T. Li, H. Zhao, X. Li, C. Gao, S. Zhang and E. Xie, *Nanoscale*, 2012, **4**, 2978-2982.
20 Z. S. Wu, W. C. Ren, L. Wen, L. B. Gao, J. P. Zhao, Z. P. Chen, G. M. Zhou, F. Li and H. M. Cheng, *Acs Nano*, 2010, **4**, 3187-3194.
21 X. Zhou, L. J. Wan and Y. G. Guo, *Adv Mater*, 2013, **25**, 2152-2157.
22 J. Yao, X. P. Shen, B. Wang, H. K. Liu and G. X. Wang, *Electrochemistry Communications*, 2009, **11**, 1849-1852.
23 D. H. Wang, R. Kou, D. Choi, Z. G. Yang, Z. M. Nie, J. Li, L. V. Saraf, D. H. Hu, J. G. Zhang, G. L. Graff, J. Liu, M. A. Pope and I. A. Aksay, *Acs Nano*, 2010, **4**, 1587-1595.
24 S. Ding, D. Luan, F. Y. C. Boey, J. S. Chen and X. W. Lou, *Chemical Communications*, 2011, **47**, 7155-7157
25 S. J. Prabakar, Y. H. Hwang, E. G. Bae, S. Shim, D. Kim, M. S. Lah, K. S. Sohn and M. Pyo, *Advanced Materials*, 2013, **25**, 3307-3312.
26 X. Zhu, Y. Zhu, S. Murali, M. D. Stoller and R. S. Ruoff, *Journal Of Power Sources*, 2011, **196**,6473-6477.
27 S. K. Park, S. H. Yu, N. Pinna, S. Woo, B. Jang, Y. H. Chung, Y. H. Cho, Y. E. Sung and Y. Piao, *Journal Of Materials Chemistry*, 2012, **22**, 2520-2525.
28 L. Wang, D. Wang, Z. Dong, F. Zhang and J. Jin, *Nano Letters*, 2013, **13**, 1711-1716.
29 J. Cheng, H. Xin, H. Zheng and B. Wang, *Journal Of Power Sources*, 2013, **232**, 152-158.
30 J. Liang, Y. Zhao, L. Guo and L. Li, *Acs Applied Materials & Interfaces*, 2012, **4**, 5742-5748.
31 X. Wang, X. Cao, L. Bourgeois, H. Guan, S. Chen, Y. Zhong, D.-M. Tang, H. Li, T. Zhai, L. Li, Y. BandoandD. Golberg, *Advanced Functional Materials*, 2012, **22**, 2682-2690.
32 W. Yue, S. Yang, Y. Ren and X. Yang, *Electrochimica Acta*, 2013, **92**, 412-420.
33 X. Zhou, Y.-X. Yin, L.-J. Wan and Y.-G. Guo, *Journal Of Materials Chemistry*, 2012, **22**, 17456-17459.
34 W. S. Hummers and R. E. Offeman, *Journal of the American Chemical Society*, 1958, **80**, 1339-1339.
35 G. M. Scheuermann, L. Rumi, P. Steurer, W. Bannwarth and R. Mulhaupt, *Journal of the American Chemical Society*, 2009, **131**, 8262-8270.
36 Y. Hong, J. Zhang, Z. Wang, J. J. Stankovich and X. Jin, *RSC Adv.*, 2014, **4**, 64402-64409.
37 D. Li, M. B. Muller, S. Gilje, R. B. Kaner and G. G. Wallace, *Nature nanotechnology*, 2008, **3**, 101-105.
38 L. S. Zhang, L. Y. Jiang, H. J. Yan, W. D. Wang, W. Wang, W. G. Song, Y. G. Guo and L. J. Wan, *Journal Of Materials Chemistry*, 2010, **20**, 5462-5467.
39 Y. Hong, Z. Wang and X. Jin, *Scientific Reports*, 2013, **3**, 3439.
40 H. He, J. Klinowski, M. Forster and A. Lerf, *Chemical Physics Letters*, 1998,**287**, 53-56.
41 R. P. Chapman, P. R. Averell and R. R. Harris, *Industrial & Engineering Chemistry*, 1943, **35**, 137-138.
42 R. Larciprete, S. Fabris, T. Sun, P. Lacovig, A. Baraldi, S. Lizzit, *J. Am. Chem. Soc.,* 2011, **133**, 17315-17321.
43 C. Zhang, X. Peng, Z. Guo, C. Cai, Z. Chen, D. Wexler, S. Li and H. Liu, *Carbon*, 2012, **50**, 1897-1903.
44 C. Xu, J. Sun and L. Gao, *Nanoscale*, 2012, **4**, 5425-5430.
45 J. S. Zhu, D. L. Wan, L. Wang, X. S. Liang and W. L. You, Electrochim. Acta 2013, **91**, 323-329.
46 J. Zhang, Z. Wang, Y. Hong, S. Li, X. Jin and G. Z. Chen, *Electrochemistry Communications*, 2014, **38**, 36-39.
47 Y. Zhu, C. Li and C. Cao, *RSC Advances*, 2013, **3**, 11860-11868.
48 T. Chen, L. Pan, X. Liu, K. Yu and Z. Sun, *RSC Advances*, 2012, **2**, 11719-11724.
49 A. H. Lim, H. W. Shim, S. D. Seo, G. H. Lee, K. S. Park and D. W. Kim, *Nanoscale*, 2012, **4**, 4694-4701.
50 Y. Li, S. Zhu, Q. Liu, J. Gu, Z. Guo, Z. Chen, C. Feng, D. Zhang and W.-J. Moon, *J. Mater. Chem.*, 2012, **22**, 2766-2773.
51 Y. Su, S. Li, D. Wu, F. Zhang, H. Liang, P. Gao, C. Cheng and X. Feng, *ACS Nano*, 2012, **6**, 8349-83.
52 J. Zhu, D. Wang, L. Wang, X. Lang and W. You, *Electrochimica Acta*, 2013, **91**, 323-329.
53 C. Zhong, J. Wang, Z. Chen and H. Liu, *The Journal of Physical Chemistry C*, 2011, **115**, 25115-25120.
54 B. Chen, H. Qian, J. Xu, L. Qin, Q. Wu, M. Zheng and Q. Dong, *Journal of Materials Chemistry A*, 2014, **2**, 9345-9352.
55 S. Li, Y. Wang, C. Lai, J. Qiu, M. Ling, W. Martens, H. Zhao and S. Zhang, *Journal of Materials Chemistry A*, 2014, **2**, 10211-10217.
56 Z. Li, G. Wu, D. Liu, W. Wu, B. Jiang, J. Zheng, Y. Li, J. Li and M. Wu, *Journal of Materials Chemistry A*, 2014, **2**, 7471-7477.
57 J. Tang, J. Yang, L. Zhou, J. Xie, G. Chen and X. Zhou, *Journal of Materials Chemistry A*, 2014, **2**, 6292-6295.
58 R. Wang, C. Xu, J. Sun, L. Gao and H. Yao, *ACS Applied Materials & Interfaces*, 2014, 6, 3427-3436.
59 J. Guo, B. Jiang, X. Zhang and H. Liu, *Journal of Power Sources*, 2014, 262, 15-22.
60 B. P. Vinayan and S. Ramaprabhu, *Journal of Materials Chemistry A*, 2013, **1**, 3865-3871.